

Variational tensor network renormalization in imaginary time: benchmark results in the Hubbard model at finite temperature

Piotr Czarnik, Marek M. Rams, and Jacek Dziarmaga

Instytut Fizyki Uniwersytetu Jagiellońskiego, ul. Łojasiewicza 11, PL-30-348 Kraków, Poland

(Dated: May 12, 2022)

A Gibbs operator $e^{-\beta H}$ for a 2D lattice system with a Hamiltonian H can be represented by a 3D tensor network, the third dimension being the imaginary time (inverse temperature) β . Coarse-graining the network along β results in an accurate 2D projected entangled-pair operator (PEPO) with a finite bond dimension. The coarse-graining is performed by a tree tensor network of isometries that are optimized variationally to maximize the accuracy of the PEPO. The algorithm is applied to the two-dimensional Hubbard model on an infinite square lattice. Benchmark results are obtained that are consistent with the best cluster dynamical mean-field theory and power series expansion in the regime of parameters where they yield mutually consistent results.

I. INTRODUCTION

Quantum tensor networks prove to be an indispensable tool to study strongly correlated quantum systems. Their history begins with an introduction of the density matrix renormalization group (DMRG)^{1,2} that was later shown to optimize the matrix product states (MPS) variational ansatz². In recent years, MPS were generalized to 2D tensor product states, also known as a projected entangled pair states (PEPS)³, as well as supplemented with the multiscale entanglement renormalization ansatz (MERA) — a refinement of the real-space renormalization group⁴. Being variational, quantum tensor networks do not suffer from the notorious fermionic sign problem and thus they can be applied to strongly correlated fermions in 2D⁵. The fermionic PEPS outperform the best variational quantum Monte Carlo (QMC) providing the most accurate results for the ground states of the $t - J^{6-9}$ and Hubbard¹⁰ models employed in the context of the high- T_c superconductivity. The networks — both MPS¹¹⁻¹³ and PEPS¹⁴⁻¹⁶ — also made major breakthroughs in the quest for topologically ordered ground states, where geometric frustration often prohibits traditional quantum Monte Carlo.

Thermal states of quantum Hamiltonians were explored with tensor networks to a lesser extent than the ground states. In 1D they can be represented by MPS prepared by accurate simulation of imaginary time evolution^{17,18} of a system with ancillas. A similar approach can in principle be applied in 2D^{19,20} — the PEPS manifold is a compact representation for Gibbs states²¹ — but the accuracy of the time evolution turns out to be problematic. Alternatively, direct contraction of the 3D tensor network representing the partition function was proposed²², but, due to local tensor update, they are expected to converge slowly with increasing refinement parameter. Any improvement towards the full update can accelerate the convergence significantly²³, which parallels similar progress in finite temperature variational quantum Monte Carlo, see e.g. Ref. 24.

In order to bypass the problems posed by simulation of imaginary time evolution, two of us introduced a vari-

ational algorithm to optimize a 2D projected entangled-pair operator (PEPO) which represents the Gibbs operator $e^{-\beta H}$ for a 2D lattice Hamiltonian H ^{25,26}. Thanks to the area law for thermal states²¹, PEPO with a finite bond dimension has a potential to be an accurate representation of the thermal state. The 2D PEPO is obtained by means of dimensional reduction from a 3D network that results from the Suzuki-Trotter decomposition of the infinitesimal time step $e^{-d\beta H}$, where $N = \beta/d\beta$ of such steps combine into the Gibbs operator. This decomposition is introducing a well controlled Trotter error which vanishes in the limit of $d\beta \rightarrow 0$. The 3D network is coarse-grained, or decimated, along the virtual (imaginary time) direction by a hierarchy of isometries. The isometries are optimized variationally — employing full tensor environments — in order to maximize the accuracy of the coarse-grained PEPO. Since the cost of the algorithm is only logarithmic in the number of time steps, the limit $d\beta \rightarrow 0$ can be easily approached for any finite β .

A benchmark application to the 2D quantum Ising model in a transverse field was presented in Ref. 25, while in Ref. 26 the same algorithm was utilized to simulate the 2D quantum compass model²⁷ — making the first step towards geometric frustration — with the results consistent with the best QMC²⁸ ones. In this paper we present the first results for the strongly correlated fermionic Hubbard model. We limit ourselves to the regime where both high temperature expansion and cluster dynamical mean-field theory give mutually consistent results collected in a review in Ref. 29, which are considered to be a benchmark for any new numerical approach. Our results meet the standards of the test.

The paper is organized as follows. In Sec. II we briefly define the Hubbard model. In Sec. III we describe the fermionic algorithm for variational renormalization and collect the numerical results in Sec. IV. We close with a discussion and conclusions in Sec. V. Finally, in the Appendix A we discuss the efficient modification of the corner transfer matrix algorithm which we employ in this work.

II. HUBBARD MODEL

The Hubbard model on an infinite square lattice is

$$H = - \sum_{\langle i,j \rangle \sigma} t \left(c_{i\sigma}^\dagger c_{j\sigma} + c_{j\sigma}^\dagger c_{i\sigma} \right) + \sum_i U n_{i\uparrow} n_{i\downarrow} + \sum_i \mu n_i, \quad (1)$$

where $c_{i\sigma}^\dagger$ and $c_{i\sigma}$, respectively, creates and annihilates an electron with spin $\sigma = \uparrow, \downarrow$ on site i , $n_{i\sigma} = c_{i\sigma}^\dagger c_{i\sigma}$ is the number operator, $n_i = n_{i\uparrow} + n_{i\downarrow}$, on-site repulsion strength $U > 0$ and the chemical potential is equal μ . $\langle i, j \rangle$ denotes summation over nearest-neighbor (NN) pairs with hopping energy $t > 0$. It is a candidate for a model describing high- T_c superconductivity which is expected to appear close to $U/t = 8$ and $n = 0.875$ at low enough temperatures. Here $n = \langle n_i \rangle$ marks average electron density per site.

For small β , the model was simulated using determinant quantum Monte Carlo (DQMC)³³ and dynamical cluster approximation (DCA)³⁴. DCA is a variant of cluster dynamical mean-field theory (DMFT) using QMC impurity solver. Both approaches exhibit the sign problem which becomes more severe for growing both β and the cluster size. It prevents from obtaining conclusive results for $\beta t > 4$ close to $U/t = 8$ and $n = 0.875$ within these approaches^{33,34}. Alternatively, for small β the model can also be simulated using high temperature series expansion, such as, e.g., numerically linked cluster expansion (NLCE)³⁵. In this article, as we are aiming to benchmark our approach, we work in the range of parameters when the above methods give mutually consistent results.

III. ALGORITHM

In this Section we describe fermionic version of the algorithm that was introduced and tested in the 2D quantum Ising model in Ref. 25 and subsequently successfully applied to the quantum compass model in Ref. 26.

A. Suzuki-Trotter decomposition

We aim at representing the Gibbs operator,

$$U(\beta) = e^{-\beta H}, \quad (2)$$

by a 2D tensor product operator shown in Figure 4c, which is also known as projected entangled-pair operator (PEPO).

To this aim we first split the evolution into N small time steps

$$U(\beta) = [U(d\beta)]^N, \quad (3)$$

where

$$N = \frac{\beta}{d\beta} \quad (4)$$

is the number of steps. Since the cost of our algorithm scales with $\log_2 N$, the step $d\beta$ can be made sufficiently small at little expense.

Since the Hamiltonian (1) is a sum of non-commuting terms, the gate $U(d\beta) = e^{-d\beta H}$ has to be approximated by the Suzuki-Trotter decomposition into a product of non-commuting Trotter gates. The on-site terms in (1) act with a gate,

$$U_U(d\beta) = \prod_i e^{-d\beta(U n_{i\uparrow} n_{i\downarrow} + \mu n_i)}, \quad (5)$$

being a product of one-site operators. In order to implement the hopping, we introduce two sublattices A and B which form a chessboard, and define hopping gates:

$$U_{AB}^\sigma(d\beta) = \prod_{\langle i_A, i_B \rangle} e^{d\beta c_{i_A\sigma}^\dagger c_{i_B\sigma}}, \quad (6)$$

$$U_{BA}^\sigma(d\beta) = \prod_{\langle i_A, i_B \rangle} e^{d\beta c_{i_B\sigma}^\dagger c_{i_A\sigma}}. \quad (7)$$

Here $\langle i_A, i_B \rangle$ marks a pair of NN sites belonging to different sublattices. These gates are products of NN two-site operators. In the second-order Suzuki-Trotter decomposition an infinitesimal imaginary time step is approximated by

$$U(d\beta) \approx U_U(d\beta/2) U_t^\uparrow(d\beta) U_t^\downarrow(d\beta) U_U(d\beta/2), \quad (8)$$

where the hopping gates are combined into two mutually commuting gates

$$U_t^\sigma(d\beta) = U_{AB}^\sigma(d\beta/2) U_{BA}^\sigma(d\beta) U_{AB}^\sigma(d\beta/2). \quad (9)$$

In order to rearrange $U_{AB}^\sigma(d\beta)$ in the form of a tensor network, at every NN bond we rewrite

$$e^{d\beta c_{i_A\sigma}^\dagger c_{i_B\sigma}} = 1 + d\beta c_{i_A\sigma}^\dagger c_{i_B\sigma} = \sum_{\nu=0,1} C_{i_A\sigma d\beta}^{\nu\dagger} C_{i_B\sigma d\beta}^\nu. \quad (10)$$

Above, $C_{i\sigma d\beta}^{\nu(\dagger)}$ is acting on site i and the bond index ν contracts two operators acting on the NN sites i_A and i_B . In the Fock basis at the site i this operator becomes a rank-3 tensor $C_{\sigma d\beta}^{(\dagger)}$ with elements:

$$C_{i\sigma d\beta}^{(\dagger)\nu mn} = \langle m | C_{i\sigma d\beta}^{\nu(\dagger)} | n \rangle. \quad (11)$$

We show its graphical representation in Fig. 1a.

B. Fermionic tensor networks

In order to represent fermionic states by tensor networks we use formalism of Ref. 6. We introduce it shortly here, while referring to Ref. 6 for a systematic derivation.

We assume that each value of each tensor index has even or odd parity, e.g., for $C_{i\sigma d\beta}^{\nu mn}$, the indices m, n are even (odd) when they label a Fock state with even (odd)

number of fermions, and even (odd) bond index $\nu = 0(1)$ corresponds to a transfer of an even (odd) number of fermions between the NN sites. It is convenient to denote the parity of an index i by $p(i)$:

$$p(i) = \begin{cases} 1 & \text{for } i \text{ even,} \\ -1 & \text{for } i \text{ odd.} \end{cases} \quad (12)$$

Then the parity of a set of indices is defined as product of their parities,

$$p(\{i_1, i_2\}) = p(i_1)p(i_2). \quad (13)$$

In the following we only work with the parity preserving tensors, i.e.,

$$T_{i_1, i_2, \dots, i_r} = 0 \quad \text{if } p(\{i_1, i_2, \dots, i_r\}) = -1. \quad (14)$$

A new feature of fermionic tensor networks are fermionic swap gates which implement fermionic anticommutators. We illustrate the general idea with an example, while a more systematic introduction can be found in Ref. 6.

Fig. 1b shows the hopping term $\sum_{\nu=0,1} C_{6\sigma d\beta}^{\dagger\nu} C_{3\sigma d\beta}^{\nu}$ from site 3 to site 6 applied to a state $|\Psi\rangle$, where the rank-9 tensor Ψ represents its amplitude in the Fock basis:

$$|\Psi\rangle = \sum_{n_1, \dots, n_9=0,1} \Psi_{n_1, \dots, n_9} (c_{1\sigma}^{\dagger})^{n_1} \dots (c_{9\sigma}^{\dagger})^{n_9} |0\rangle \quad (15)$$

For odd $\nu = 1$ we have $C_{3\sigma d\beta}^{\nu} \sim c_{3\sigma}$ and the intermediate state $c_{3\sigma}|\Psi\rangle$ is

$$\sum_{n_1, \dots, n_9=0,1} \Psi_{n_1, \dots, n_9} (-1)^{n_1} (-1)^{n_2} \delta_{1, n_3} (c_1^{\dagger})^{n_1} (c_2^{\dagger})^{n_2} (c_3^{\dagger})^0 \dots (c_9^{\dagger})^{n_9} |0\rangle. \quad (16)$$

Thanks to fermionic anticommutators, the amplitude acquires a factor $(-1)^{n_1}(-1)^{n_2}$. This factor can be taken into account in the tensor network formalism by introduction of swap gates.

A swap gate is a rank 4 tensor $s_{i,i',j,j'}$:

$$s_{i,j,i',j'} = \delta_{i,i'} \delta_{j,j'} S(i, j), \quad (17)$$

where

$$S(i, j) = \begin{cases} -1 & \text{for } p(i) = p(j) = -1, \\ 1 & \text{otherwise.} \end{cases} \quad (18)$$

Its graphical representation is shown in Fig. 1b.

The factor $(-1)^{n_1}(-1)^{n_2}$ from Eq. (16) (see Fig. 1c) is represented by the two swap gates appearing at the crossing of the bond-index ν (black lines in the figure) coming from the tensor $C_{3\sigma d\beta}$ and the fermionic indices at sites 1 and 2 (red lines). For $\nu = 1$ the two gates in Fig. 1c produce the required factor. The action of the hopping term is completed by applying $C_{6\sigma d\beta}^{\dagger\nu}$ at site 6. Its application produces, for $\nu = 1$, another factor

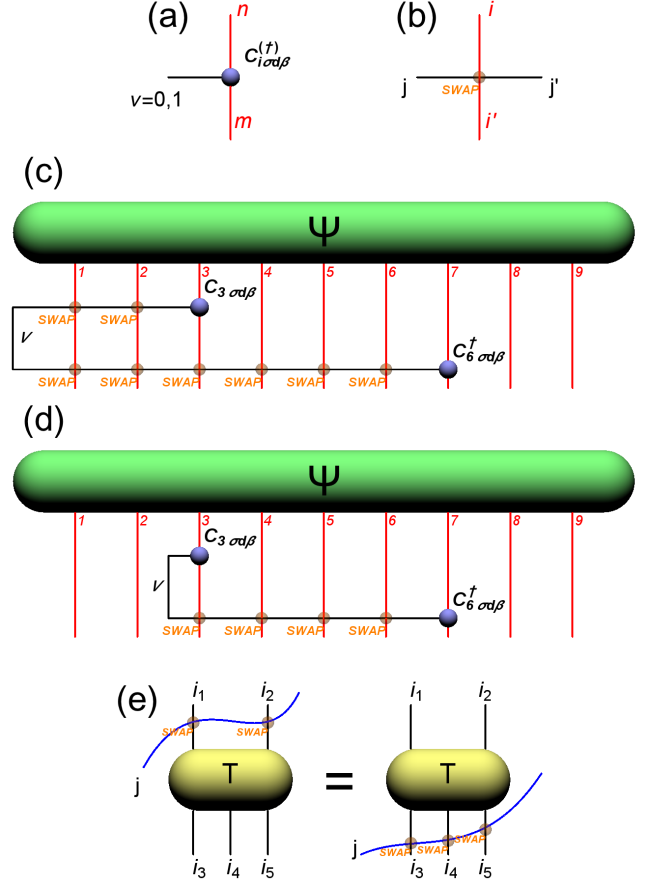


FIG. 1. (Color online) In (a), graphical representation of fermionic tensor $C_{i\sigma d\beta}^{(\dagger)}$ with elements $C_{i\sigma d\beta}^{(\dagger)\nu mn} = \langle m | C_{i\sigma d\beta}^{\nu(\dagger)} | n \rangle$ for site i and spin σ . The black line represents the bond index ν connecting this operator with a NN site along the bond. The red lines represent indices m and n numbering Fock states at site i . In (b) graphical representation of the swap gate $s_{i,j,i',j'} = \delta_{i,i'} \delta_{j,j'} S(i, j)$, where $S(i, j) = -1$ if both values of indices i and j are odd and $S(i, j) = 1$ otherwise. In (c), the hopping gate $\sum_{\nu} C_{6\sigma d\beta}^{\dagger\nu} C_{3\sigma d\beta}^{\nu}$ is applied to a quantum state $|\Psi\rangle$. At every crossing of the bond index $\nu = 0, 1$ (black line) with a fermionic index (red lines), there is a fermionic swap gate. The gate produces factor -1 when both values of the crossing indices are odd and factor 1 otherwise. Here each of the red indices is odd when it labels a Fock state with an odd number of fermions. The bond index is odd when it labels a transfer of an odd number of fermions between sites ($\nu = 1$ here). In (d), the pairs of swap gates at sites 1 and 2 cancel out so the bond line can be shortened. In (e), an example of freedom in choosing tensor network representations of fermionic systems is shown. The index j (the blue line) can be dragged over a parity preserving tensor T without changing factors produced by the swap gates.

$(-1)^{n_1}(-1)^{n_2} \dots (-1)^{n_6}$. This factor is represented in Fig. 1c by swap gates at the crossings of the (black) bond index ν and (red) fermionic indices $1, 2, \dots, 6$.

To summarize, for $\nu = 1$ we obtained in total two factors $(-1)^{n_1}$ and two factors $(-1)^{n_2}$ which, respectively,

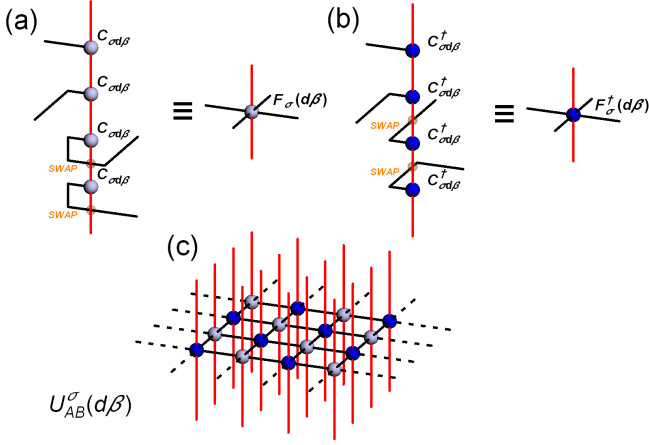


FIG. 2. (Color online) In (a), four operators $C_{i\sigma d\beta}^{\nu}$ are applied at site i (not shown). Each operator has one bond index connecting it with an operator $C_{j\sigma d\beta}^{\nu}$ at a NN site j . The whole diagram can be represented by a compact rank-6 tensor $F_{\sigma}(d\beta)$. In (b) four operators $C_{i\sigma d\beta}^{\nu\dagger}$ are represented by a rank-6 tensor $F_{\sigma}^{\dagger}(d\beta)$. In (c) the gate $U_{AB}^{\sigma}(d\beta)$ in Eq. (19) is a chessboard constructed from $F_{\sigma}(d\beta)$ and $F_{\sigma}^{\dagger}(d\beta)$, where each line connecting two NN tensors at sites i_A and i_B represents contraction of their common bond index $\nu_{i_A i_B}$ and each line crossing implies a swap factor (not shown).

cancel out. This corresponds to cancellation of two swap gates between the same pairs of indices. Therefore we can remove swap gates at the crossings of the fermionic indices 1 and 2 with the bond index ν , and obtain the final tensor network representation of the hopping term in Fig. 1d.

In the following any crossing of two lines implies a swap gate between the corresponding indices. For the sake of clarity, starting from Figure 2c on we do not show the swap gates explicitly.

Finally, Fig. 1e illustrates the advantage which results from using parity preserving tensors. In Fig. 1e a parity preserving tensor $T_{i_1, i_2, i_3, i_4, i_5}$ is swapped with an index j (the blue line) in two equivalent ways. The left and right diagrams denote respectively $\sum_{i'_1, i'_2, j'} T_{i'_1, i'_2, i_3, i_4, i_5} s_{i_1, j, i'_1, j'} s_{i_2, j', i'_2, j''}$ and $\sum_{i'_3, i'_4, i'_5, j', j''} T_{i_1, i_2, i'_3, i'_4, i'_5} s_{i_3, j, i'_3, j'} s_{i_4, j', i'_4, j''} s_{i_5, j'', i'_5, j''}$. Because $T_{i_1, i_2, i_3, i_4, i_5}$ is a parity preserving tensor then by definition it is only nonzero for $p(i_1, i_2) = p(i_3, i_4, i_5)$, which in turns implies that for each given value of j index a factor introduced by the swap gates between j index and i_1, i_2 indices is the same as a factor introduced by the swap gates between j index and i_3, i_4, i_5 indices. Therefore we can drag the blue line over the tensor. In the following we frequently drag indices over tensors to optimize cost of tensor contractions.

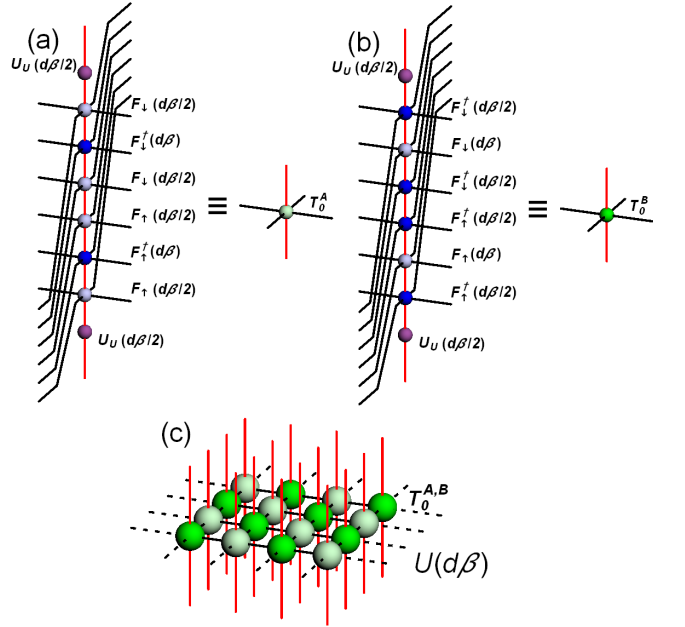


FIG. 3. (Color online) In (a), F and F^{\dagger} on sublattice A are combined into a single elementary Trotter tensor T_0^A according to Eqs. (8,9). Each bond index of new T_0^A has dimension 2^6 . In (b), similar operation is performed for sublattice B. In (c), a layer of the elementary Trotter tensors forms the infinitesimal gate $U(d\beta)$ and N such layers put on top of each other represent the Gibbs operator $U(\beta)$ in Eq. (3).

C. Hopping gates

Now we can proceed with rewriting the hopping gate as a contraction of tensors via their bond indices:

$$U_{AB}^{\sigma}(d\beta) = \prod_{\langle i_A, i_B \rangle} e^{d\beta} c_{i_A \sigma}^{\dagger} c_{i_B \sigma} = \sum_{\{\nu\}} \prod_{\langle i_A, i_B \rangle} C_{i_A \sigma d\beta}^{\dagger \nu_{i_A i_B}} C_{i_B \sigma d\beta}^{\nu_{i_A i_B}} \quad (19)$$

Here $\nu_{i_A i_B}$ is a bond index along NN bond $\langle i_A, i_B \rangle$ and $\{\nu\}$ is a set of all such bond indices. In Fig. 2a, four operators $C_{i_B \sigma d\beta}^{\nu}$ are combined into a single rank-6 tensor $F_{\sigma}(d\beta)$. In Fig. 2b, four operators $C_{i_A \sigma d\beta}^{\nu\dagger}$ are combined into $F_{\sigma}^{\dagger}(d\beta)$. In Fig. 2c, a chessboard layer of $F_{\sigma}(d\beta)$ and $F_{\sigma}^{\dagger}(d\beta)$ is shown representing the gate $U_{AB}^{\sigma}(d\beta)$. The other gate $U_{BA}^{\sigma}(d\beta)$ is a similar layer but with $F_{\sigma}(d\beta)$ and $F_{\sigma}^{\dagger}(d\beta)$ interchanged.

According to Eq. (9), a sandwich of three such chessboard layers on top of each other is the hopping gate U_t^{σ} . Following from Eq. (8), two such sandwiches on top of each other, dressed at both ends with the on-site gates U_U , combine into the infinitesimal gate $U(d\beta)$. In practice, it is not possible to contract such 3D layered networks exactly and, therefore, we proceed by contracting them along their Fock indices first. This is presented in Figs. 3a and b, where the operators corresponding to

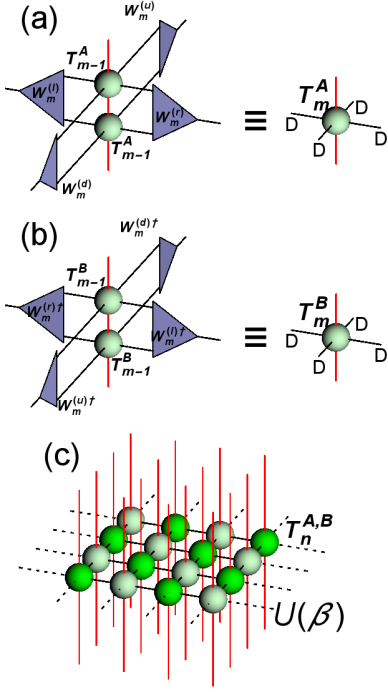


FIG. 4. (Color online) In (a), a coarse-graining step along virtual (imaginary time) direction, where two Trotter tensors T_{m-1}^A are combined and renormalized into a single tensor T_m^A by four isometries $W_m^{(u)}, W_m^{(r)}, W_m^{(d)}, W_m^{(l)}$. Similarly, in (b), isometries $W_m^{(u)†}, W_m^{(r)†}, W_m^{(d)†}, W_m^{(l)†}$ renormalize corresponding indices of a combination $T_{m-1}^B \times T_{m-1}^B \rightarrow T_m^B$. Finally, PEPO tensors T_n^A and T_n^B result from n such coarse-graining transformations. In (c), a chessboard layer of contracted $T_n^{A,B}$ forms the PEPO ansatz for the Gibbs operator $U(\beta)$.

sublattices A and B , are combined into elementary Trotter tensors T_0^A and T_0^B , respectively. To that end, the 6 bond indices along each direction on the lattice are fused together into a single bond index of dimension 2^6 . A layer of such tensors, shown in Fig. 3c, represents the infinitesimal gate $U(d\beta)$ in Eq. (19), up to the Trotter error controlled by $d\beta$. Finally, the evolution operator $U(\beta)$ in Eq. (3) is obtained by placing N such layers on top of each other.

D. Coarse graining and renormalization in imaginary time

Equation (3) suggests to combine N elementary tensors T_0^A or T_0^B into a single PEPO tensor in a similar way as in Figs. 3a or b, where six tensors were combined into a single Trotter tensor T_0^A or T_0^B . Unfortunately, we cannot proceed along these lines anymore as this would require fusing N bond indices along each lattice direction, each of dimension 2^6 , into a single bond index of dimension 2^{6N} .

In order to avoid this exponential blow-up in N , we prefer to proceed step-by-step, each time combining just

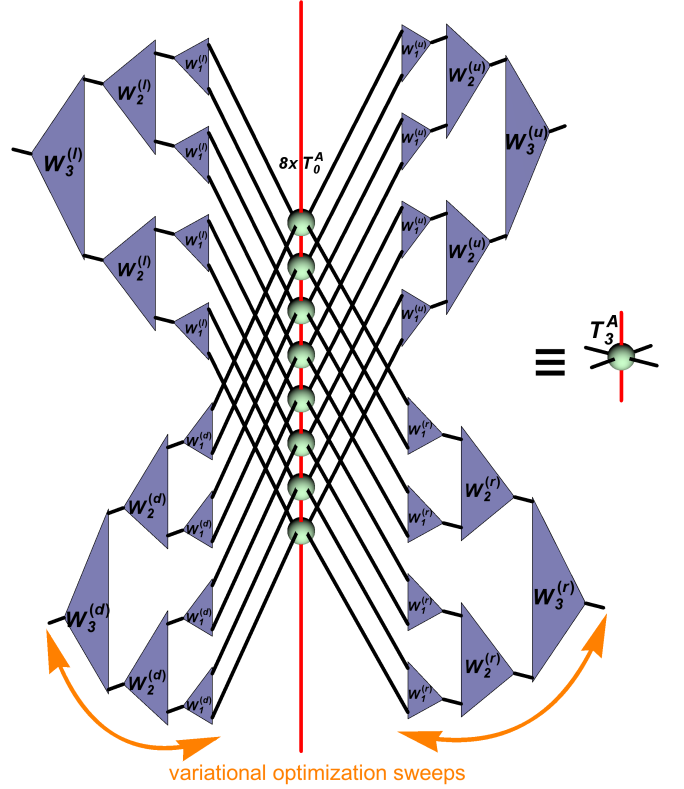


FIG. 5. (Color online) Three coarse-graining transformations in Fig. 4c result in a Trotter tensor T_3^A . After dragging the lines coming from the eight elementary T_0^A over the isometries, like in Fig. 1e, the isometries acting along a given bond combine into a tree tensor network (TTN). They are optimized by repeated up- and down-sweeps.

two tensors into one and renormalizing the bond indices: $T_0^{A,B} \times T_0^{A,B} \rightarrow T_1^{A,B}, \dots, T_{n-1}^{A,B} \times T_{n-1}^{A,B} \rightarrow T_n^{A,B}$, where

$$n = \log_2 N = \log_2 \frac{\beta}{d\beta} \quad (20)$$

is the total number of transformations. It is scaling logarithmically in the total number of Suzuki-Trotter steps N or, equivalently, in $d\beta$.

After each fusion of two tensors, $T_{m-1}^{A,B} \times T_{m-1}^{A,B} \rightarrow T_m^{A,B}$, the two bond indices along each lattice direction are renormalized down to D using four isometries: $W_m^{(u)}, W_m^{(r)}, W_m^{(b)}, W_m^{(l)}$, as shown in Figs. 4a and b. This renormalization keeps the bond dimension fixed at a tractable D . Figure 5, for instance, shows the net outcome after 3 such coarse-graining transformations. Along each bond there are 3 layers of isometries: W_1, W_2, W_3 , that combine into structure of a tree tensor network (TTN)³⁰.

After n coarse-graining steps we obtain tensors $T_n^{A,B}$. Their chessboard layer shown in Fig. 4c is the PEPO Ansatz for the gate $U(\beta)$. In the final n -th renormalization we insert a trivial isometry (the identity) increasing

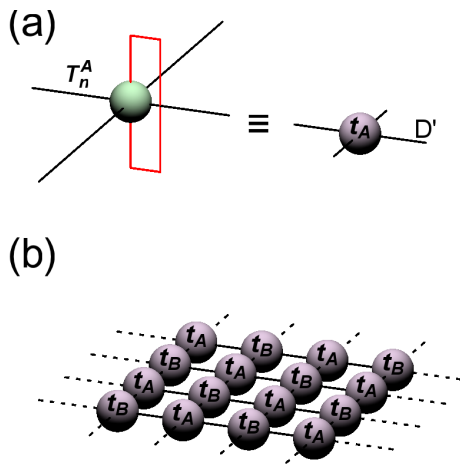


FIG. 6. (Color online) In (a), tracing out the (red) fermionic indices of tensor T_n^A forms a transfer tensor t_A . In (b), chessboard layer of contracted transfer tensors t_A and t_B represents the partition function $Z = \text{Tr} U(\beta) = \text{Tr} e^{-\beta H}$.

the bond dimension to

$$D' = D^2 \quad (21)$$

to minimize effects of the final truncation.

The partition function $Z = \text{Tr} e^{-\beta H}$ is a trace of the PEPO. It can be represented by a chessboard in Fig. 6b formed by transfer tensors t_A and t_B . The transfer tensors are obtained by tracing out fermionic indices of corresponding PEPO tensors $T_n^{A,B}$, see Fig. 6a. These rank-4 transfer tensors have only bond indices with the bond dimension D' .

E. Figure of merit

Figure 5 shows the net outcome after 3 renormalization steps. There is a central column of 2^3 elementary Trotter tensors T_0^A . Their indices in the direction of bond x are renormalized down to the bond dimension D by 3 layers of isometries $W_m^{(x)}$. The isometries form a tree tensor network that is also an isometry. A similar picture could be drawn for the total of n coarse-graining steps with a column of $N = 2^n$ elementary T_0^A in the center and n layers of isometries $W_m^{(x)}$ in each tree tensor network. Therefore, as shown in Fig. 7a, the transfer tensor t_A is effectively obtained from a huge tensor T^A , where T^A is the central column of N tensors T_0^A traced over its (red) fermionic indices. The same is true for t_B , see Fig. 7b. Consequently, any contraction of t_A with t_B corresponds to insertion of an orthogonal projector at every contracted bond index of T^A and T^B , see Fig. 7c. Such a projector is inserted e.g. at every bond index of the partition function in Fig. 6b. If this projector were an identity, the network in Fig. 6b would be the exact partition function. Since it projects onto a small

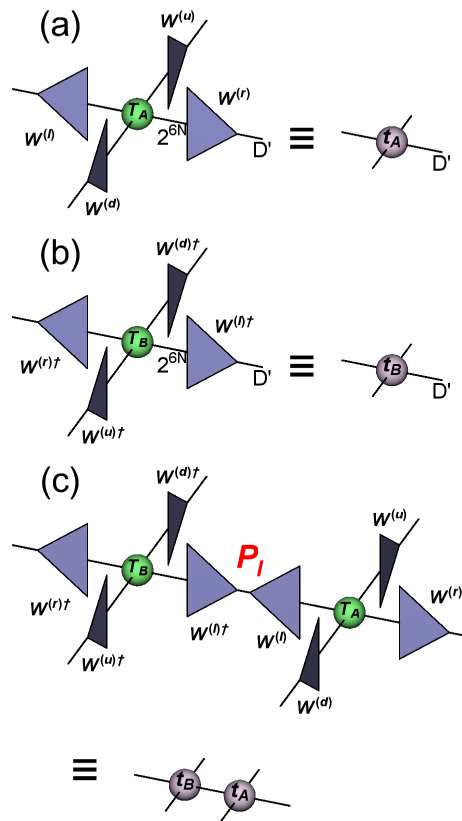


FIG. 7. (Color online) In (a), the transfer tensor t_A is obtained from a tensor T^A made of N elementary tensors T_0^A , see Figs. 5 and 6a. A bond dimension of T_A is renormalized from huge 2^{6N} down to D' . The renormalization along lattice bond x is done by an isometry $W^{(x)}$, where $x = l, r, u, d$. The huge isometry is a tree tensor network of small isometries $W_m^{(x)}$, compare Fig. 5. In (b), the transfer tensor t_B has a similar structure as t_A . In (c), any contraction along a bond between t_A and t_B , like in the partition function in Fig. 6b, involves an orthogonal projector inserted between T^A and T^B . Here the tensors are contracted along their common l -bond and the projector is $P_l = W^{(l)†}W^{(l)}$.

D' -dimensional subspace, the isometries have to be optimized to minimize distortion of the partition function by projectors. The distortion is minimized by maximizing the figure of merit we shall construct now.

Figure 8a defines l -bond environment e_l which is the partition function in Fig. 6c but with one of its l -bonds left uncontracted. The uncontracted bond corresponds to “cutting” in half the projector $P_l = W^{(l)†}W^{(l)}$ introduced in Fig. 7c. Therefore, the $D' \times D'$ -dimensional bond environment e_l can be rewritten as

$$e_l = W^{(l)} E_l W^{(l)†}, \quad (22)$$

where we formally introduce a $2^{6N} \times 2^{6N}$ unrenormalized bond environment E_l . We want to minimize the distortion of E_l by the isometries in Eq. (22) or, equivalently, we want a projected environment $W^{(l)†}W^{(l)} E_l W^{(l)†}W^{(l)} = P_l E_l P_l$ to be as close to the

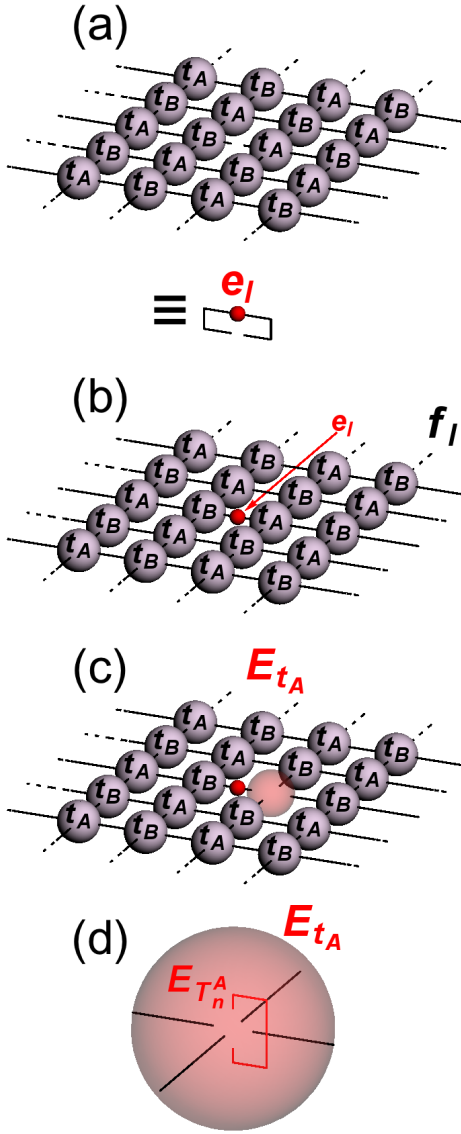


FIG. 8. (Color online) In (a), a bond environment e_l is obtained after cutting one of l -bonds in the partition function in Fig. 6c. In (b), the figure of merit f_l in Eq. (24) is obtained by inserting a tensor representing e_l into the cut bond in panel (a). In (c), tensor environment E_{t_A} for the tensor t_A adjacent to the optimized l -bond is obtained by removing the adjacent t_A from the figure of merit in panel (b). In (d), tensor environment $E_{T_n^A}$ for PEPO tensor T_n^A is obtained from E_{t_A} .

original E_l as possible. To this end we minimize the difference

$$\begin{aligned} & \text{Tr} (P_l E_l P_l - E_l)^\dagger (P_l E_l P_l - E_l) = \\ & \text{Tr} E_l^\dagger E_l - \text{Tr} E_l^\dagger P_l E_l P_l = \\ & \text{Tr} E_l^\dagger E_l - \text{Tr} e_l^\dagger e_l, \end{aligned} \quad (23)$$

where we used $P_l P_l = P_l = P_l^\dagger$, $P_l = W^{(l)\dagger} W^{(l)}$, and Eq. (22). Since E_l does not depend on the isometries $W^{(l)}$ at the considered l -bond, the first term in (23) is constant

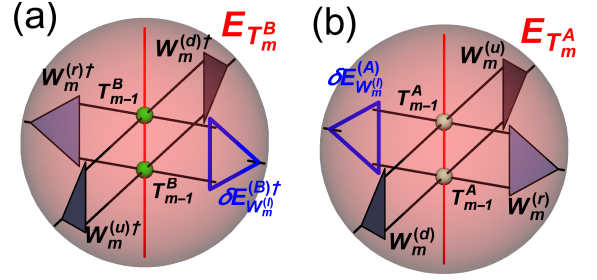


FIG. 9. (Color online) There are two inequivalent contributions to the tensor environment of isometry $W_m^{(l)}$: $\delta E_{W_m^{(l)}}^{(B)}$ from sublattice B in panel (a) and $\delta E_{W_m^{(l)}}^{(A)}$ from sublattice A in panel (b). They add up to form a full environment $E_{W_m^{(l)}} = \delta E_{W_m^{(l)}}^{(A)} + \delta E_{W_m^{(l)}}^{(B)}$.

with respect to these isometries and the actual figure of merit is

$$f_l = \text{Tr} e_l^\dagger e_l. \quad (24)$$

It has to be maximized with respect to isometries $W_m^{(l)}$ at the considered l -bond. Diagrammatically, f_l can be obtained after inserting a tensor representing e_l^\dagger into the uncontracted bond of the network representing e_l , as shown in Fig. 8b.

Due to translational invariance, the same isometries $W_m^{(l)}$ appear at every l -bond in the infinite tensor network representing the partition function. They are optimized iteratively: once the $W_m^{(l)}$ at the considered l -bond are optimized, the optimized $W_m^{(l)}$ are applied at all equivalent l -bonds of the partition function. The iteration is repeated until self-consistency between different l -bonds is achieved. Similar FOM's are simultaneously maximized for the other three bonds: f_r , f_u , and f_d . The optimization is iterated until self-consistency between different types of bonds is also achieved.

F. Variational optimization

A preparatory step for variational optimization of isometries is calculation of the bond environment e_l in Fig. 8a. This infinite network cannot be contracted exactly, but its accurate approximation, that can be improved in a systematic way, is obtained with the corner transfer matrix method (CTM)³¹. We described the modification of the CTM algorithm of Ref. 8, which we employ here, in the Appendix A. Similar calculations are done in parallel to obtain e_r , e_u and e_d .

In order to optimize f_l with respect to an isometry $W_m^{(l)}$ at the considered l -bond, we need a derivative of f_l with respect to this isometry. Since f_l is a composed function, we calculate first derivatives of f_l with respect to the two

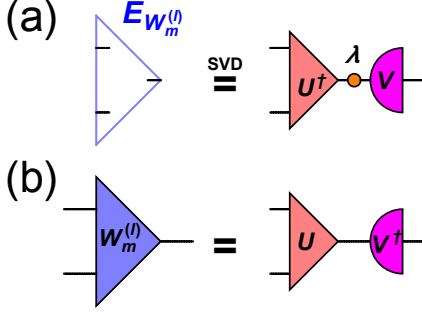


FIG. 10. (Color online) An update of isometry $W_m^{(l)}$, where the figure of merit $f_l \propto \text{Tr} W_m^{(l)} E_{W_m^{(l)}}$. In (a), the environment is subject to singular value decomposition: $E_{W_m^{(l)}} = V\lambda U^\dagger$. In (b), the isometry is updated as $W_m^{(l)} = UV^\dagger$.

transfer tensors, t_A and t_B , adjacent to the l -bond. The derivatives are proportional to the tensor environments E_{t_A} and E_{t_B} that are obtained by removing from f_l the adjacent t_A and t_B , respectively. The construction of E_{t_A} is shown in Fig. 8c. E_{t_B} is constructed in an analogous way.

With E_{t_A} at hand, it is easy to construct an environment $E_{T_n^A}$ of the PEPO tensor T_n^A , see Fig. 8d. $E_{T_n^A}$ is proportional to a derivative of f_l with respect to the T_n^A adjacent to the l -bond that we want to optimize. A similar step from E_{t_B} to $E_{T_n^B}$ is done in parallel. With both $E_{T_n^A}$ and $E_{T_n^B}$ at hand, a down optimization sweep for isometries $W_m^{(l)}$ can be initialized.

From, respectively, $E_{T_n^A}$ and $E_{T_n^B}$ two contributions, $\delta E_{W_n^{(l)}}^{(A)}$ and $\delta E_{W_n^{(l)}}^{(B)}$, to the environment $E_{W_n^{(l)}}$ are obtained, see Fig. 9. They add up to a full environment, $E_{W_n^{(l)}} = \delta E_{W_n^{(l)}}^{(A)} + \delta E_{W_n^{(l)}}^{(B)}$. The environment $E_{W_n^{(l)}}$ is used immediately to update $W_n^{(l)}$ by singular value decomposition, see Fig. 10.

With the updated $W_n^{(l)}$ the first step down in the TTN hierarchy can be done from $E_{T_n^{A,B}}$ to $E_{T_{n-1}^{A,B}}$, see Fig. 11. Then new environments $E_{W_{n-1}^{(l)}}$ are obtained from $E_{T_{n-1}^{A,B}}$ and used immediately to update the isometries $W_{n-1}^{(l)}$. The same procedure is repeated all the way down to $W_1^{(l)}$ whose update completes the down-sweep.

Once $W_1^{(l)}$ and $T_1^{A,B}$ are updated, an up optimization sweep begins. It has n steps. In the m -th step the tensors $T_{m-1}^{A,B}$ and the environments $E_{T_{m-1}^{A,B}}$ — calculated before during the down-sweep — are contracted to obtain the environments $E_{W_m^{(l)}}$ and update the isometries $W_m^{(l)}$, see Fig. 9. The updated $W_m^{(l)}$ are used to coarse-grain $T_{m-1}^{A,B} \times T_{m-1}^{A,B} \rightarrow T_m^{A,B}$, see Figs. 4b,c. This basic step is repeated all the way up to T_n .

The up-sweep completes one optimization loop consisting of three stages:

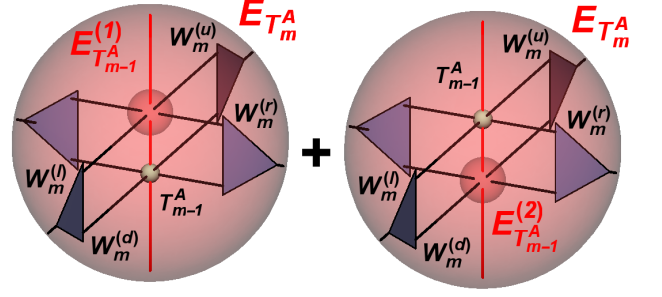


FIG. 11. (Color online) There are two inequivalent contributions to the environment of T_{m-1}^A : $E_{T_{m-1}^A}^{(1)}$ and $E_{T_{m-1}^A}^{(2)}$, which add up to form the full environment $E_{T_{m-1}^A} = E_{T_{m-1}^A}^{(1)} + E_{T_{m-1}^A}^{(2)}$.

- the CTM procedure:

$$T_n^{A,B} \xrightarrow{\text{CTM}} E_{t_{A,B}} \rightarrow E_{T_n^{A,B}};$$

- the down-sweep:

$$E_{T_n^{A,B}} \rightarrow E_{W_n^{(l)}} \rightarrow E_{T_{n-1}^{A,B}} \rightarrow \dots \rightarrow E_{T_1^{A,B}} \rightarrow E_{W_1^{(l)}};$$

- the up-sweep:

$$T_0^{A,B} \rightarrow T_1^{A,B} \rightarrow E_{W_2^{(l)}} \rightarrow T_2^{A,B} \rightarrow \dots \rightarrow E_{W_n^{(l)}} \rightarrow T_n^{A,B}.$$

Here each $E_{W_m^{(l)}}$ is used immediately to update $W_m^{(l)}$. Similar optimization sweeps are done in parallel for $W_m^{(r)}$, $W_m^{(u)}$ and $W_m^{(d)}$. The loop is repeated until convergence. The dominant numerical cost of the procedures in this section scales like D^8 . Typically, it is subleading as compared to the cost of CTM.

Having outlined the algorithm we can now proceed with the benchmark results for the Hubbard model.

IV. BENCHMARK RESULTS

A. Non-interacting case

We begin testing our algorithm in an exactly solvable version of the Hamiltonian (1) without the interaction term, $U = 0$, and with only one specie of spin-less fermions. The thermal state is the finite-temperature Fermi sea which, while being a trivial product state in the quasi-momentum basis, for large β is strongly entangled in the position representation and therefore pose a challenge for tensor networks.

Numerical results for the inverse temperature $\beta t = 2.56$ are collected in Fig. 12. We show results for the

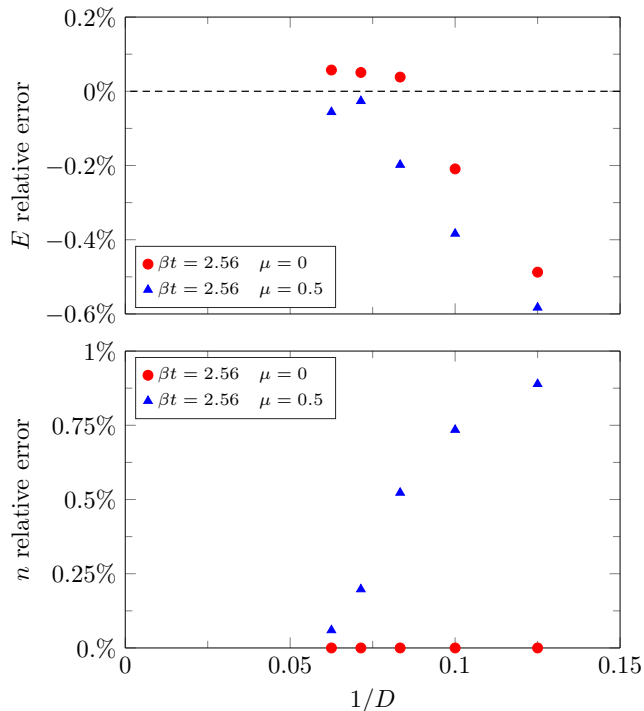


FIG. 12. (Color online) Relative errors of energy E and average fermion density n for non-interacting spinless fermions at temperature $\beta t = 2.56$ and two values of chemical potential as a function of the bond dimension $8 \leq D \leq 16$.

chemical potential $\mu = 0$ and $\mu = 0.5$. We present relative errors of energy E and fermion density n . E is defined as energy per site where we neglect the contribution related to the chemical potential – this is done in order to match convention of Ref. 29. We see systematic improvement with growing bond dimension D , with the relative error below 0.1% for the largest $D = 16$ used here.

B. Strongly correlated case

Finally, to benchmark our algorithm we simulate strongly correlated case of $U/t = 8$. We collect the results at inverse temperatures $\beta t = 1$ and $\beta t = 2$, and for electron densities $n = 1, 0.875$, and 0.85 in Fig. 13. We compare them with DCA results which are obtained by extrapolating the cluster size to infinity^{29,36}. The DCA results at $n = 1, \beta t = 1, 2$ and $n = 0.85, \beta t = 1$ were shown to be consistent with NLCE and DQMC results^{29,36}, so they can be treated as a benchmark. With the increasing bond dimension D our results approach those obtained by DCA. For the largest simulated $D = 20$ the energies E (the double occupancies $\langle n_{i,\uparrow} n_{i,\downarrow} \rangle$) agree well with DCA as relative discrepancies are smaller than 1.9% (3.6%).

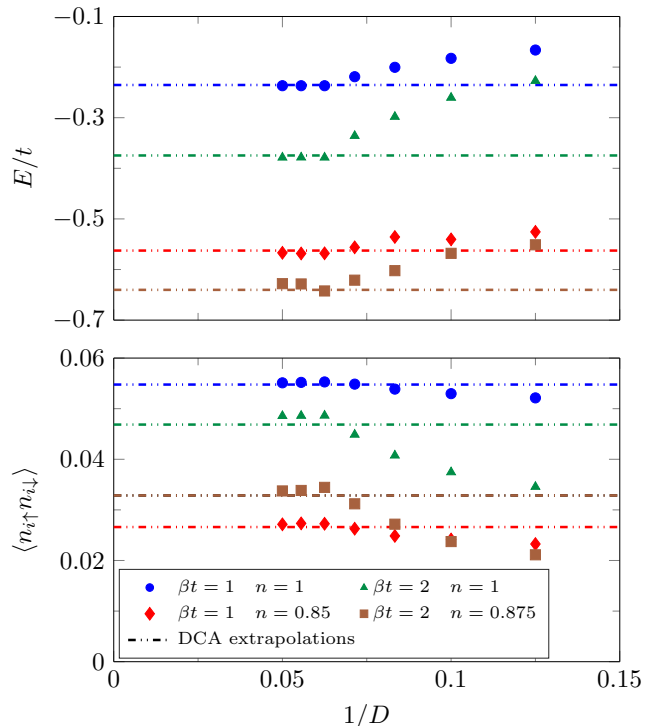


FIG. 13. (Color online) Points show total energy E and double occupancy $\langle n_{i,\uparrow} n_{i,\downarrow} \rangle$ as a function of the bond dimension $8 \leq D \leq 20$ obtained for the Hubbard model in Eq. (1) for $U/t = 8$. Circles, triangles, squares and diamonds mark different temperatures or electron densities. Errors of electron density n for the given bond dimension D , related to scanning for the correct value of the chemical potential μ , are smaller than 0.001. For comparison, lines show corresponding results from dynamical cluster approximation calculations extrapolated with the cluster size sent to infinity^{29,36}.

C. Numerical details

All simulations were made with MATLAB using *ncon* tensor network contractor³² and representing tensors with real numbers. The results for $U/t = 8$ were obtained using 3 desktops during 3 weeks.

The results were already converged in the environmental bond dimension M (see Appendix A) for $M = 30$ in the case of $U/t = 8$ and for $M = 50$ in the non-interacting case. They are also converged in the small Trotter step $d\beta$ for $d\beta t \leq 0.001$.

V. CONCLUSION

In this paper we presented a fermionic version of the algorithm that was introduced and tested in the 2D quantum Ising model in Ref. 25 and applied to the quantum compass model in Ref. 26. The Gibbs operator $e^{-\beta H}$ for a 2D lattice system can be represented by a 3D tensor network, where the third dimension is the imaginary

time (inverse temperature) β . Thanks to the area law for thermal states, coarse-graining the 3D network along β results in an accurate 2D projected entangled-pair operator (PEPO) with a finite bond dimension D' . The coarse-graining is performed by a tree tensor network (TTN) of isometries that are optimized variationally to maximize the accuracy of the final PEPO.

Here the algorithm was applied to the fermionic Hubbard model on an infinite square lattice. Results were obtained at $\beta t = 1$ and $\beta t = 2$ for electronic densities $n = 1, 0.85$, and 0.875 . In this regime different numerical methods (DCA, NLCE, DQMC) yield mutually consistent results that are considered to be a benchmark test for any new algorithm²⁹. The results in this paper demonstrate that our method meets these standards.

The fermionic algorithm presented here is largely a straightforward generalization of the algorithm developed for spin models^{25,26}. The necessary modification are the – by now standard – swap gates that account for the anti-commuting character of the degrees of freedom. A novel algorithmic feature of this paper is a numerically efficient modification of corner matrix renormalization algorithm that, however, is a general development not addressing any specific needs of the strongly correlated fermions. While the current approach is yielding promising results there is still room for further algorithmic improvements, for instance in the design of dimensional reduction scheme which is limited to orthogonal projectors in the current approach.

ACKNOWLEDGMENTS

We kindly acknowledge support by Narodowe Centrum Nauki (National Science Center) under Project No. 2013/09/B/ST3/01603. The work of P.C. on his Ph.D. thesis was supported by Narodowe Centrum Nauki under Project No. 2015/16/T/ST3/00502.

Appendix A: Corner transfer matrix renormalization

The numerically most expensive part of the algorithm is computation of the environment of a single bond in Fig. 8a. We employ the modified version of the corner-transfer-matrix renormalization (CTM) algorithm described in Ref. 8. The alternation boils down to the strategy of finding the projectors which renormalize enlarged CTM corner and edge tensors, which, while being significantly less expensive, turns out to be numerically almost as stable as the original one. For completeness, in Fig. 14 we illustrate all steps making up a single CTM update for a network with unit cell on a chessboard used in Fig. 8a.

The CTM algorithm computes corner $C^{nw}, C^{ne}, C^{se}, C^{sw}$ and edge T^n, T^e, T^s, T^w tensors which encode the infinite two-dimensional network surrounding bulk tensors t , as shown in Fig. 14(a),

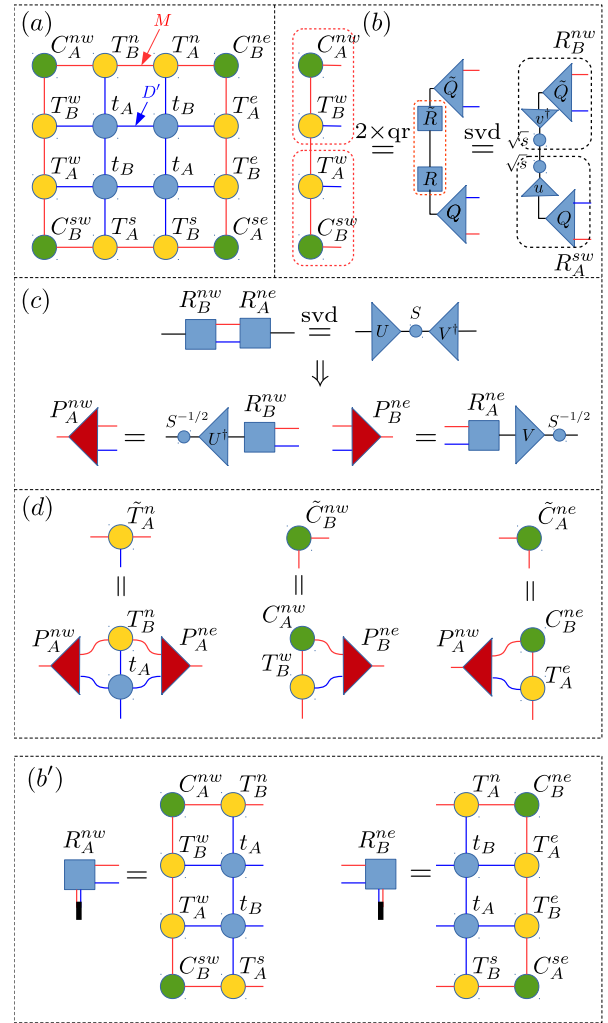


FIG. 14. (Color online) Details of a single up move in the corner transfer matrix algorithm. (a) A block of 2×2 $t_{A(B)}$ tensors on a chessboard, where its environment is represented by environment tensors C and T . (b) West half-plane is divided using SVD with singular values split symmetrically between the two parts. Performing QR decomposition in the middle step increases efficiency. The same is done for east half-plane (not shown). (c) SVD of $R_A^{nw} R_B^{ne}$ (and similarly $R_B^{nw} R_A^{ne}$) is performed to find the projectors P , which, in (d), are used to truncate the enlarged edge and corner tensors. Step (b) replaces (b') from Ref. 8. If (b') is used instead, additionally, only M largest singular values are kept to calculate projectors in (c).

where the subscript $A(B)$ labels the position in the unit cell. We refer to Ref. 8 for the details of the method and focus here on differences.

Fig. 14(b)-(d) shows how to perform the up (north) move. In Fig. 14b we divide the enlarged environment corresponding to west half-plane into the north-west R^{nw} and the south-west R^{sw} parts using SVD where singular values are symmetrically split between the two parts. For a choice of effective half-plane in Fig. 14(b) we exploit that it is not full-rank: by computing the QR de-

composition as a middle step, we are left with SVD of $M \times M$ matrix, instead of not-full-rank $D'M \times D'M$ matrix. Similarly, we divide east half-plane into R^{ne} and R^{se} (not shown). This substitutes the step (b') used in Ref. 8. Matrices R^{nw} and R^{ne} are then used in (c) to compute the projectors P^{nw} and P^{ne} . Finally, in (d) we update the north edge and corner tensors by using the projectors P to truncate the enlarged old ones. This completes single up move. The down and up moves on both sublattices A and B are all performed simultaneously. The procedure is then run iteratively performing up-down and left-right moves until convergence.

We note that in step (b) R^{nw} etc. are $M \times D'M$ matrices, so one only needs to find SVD of $M \times M$ matrix to calculate projectors in (c), comparing to SVD of $D'M \times D'M$ matrix if (b') is used instead. This way, for the range of $D' = D^2 \leq 20^2$ used in this article the numerically most expensive part of the modified CTM update becomes the renormalization of the edge tensor in step (d). From our experience the above procedure is almost as stable as the original one and within the precision of the main algorithm converges to the same values of local observables. What is more, the singular values obtained in step (c) are typically by a factor of square root larger than when (b') is used instead, which suggest better numerical stability of calculating the projectors P (where the singular values are inverted) – we however don't see that this is of relevance within the required precision.

The biggest disadvantage of using step (b) is that it does not allow to systematically increase the bond-dimension M of corner and edge tensors in a single CTM step. That is why we find it optimal to combine the two

strategies and perform a single expensive move using (b') after every 10–20 moves using (b), where we observe that the two strategies are complementary in a sense that typically the procedure is monotonically converging. While greatly reducing the time needed for CTM to converge this provides systematic way of increasing the CTM bond dimension M to converged in.

The procedure can be understood as analogical to the truncation in infinite Matrix Product State (iMPS)³⁷ – in principle biorthogonal³⁸ as the Matrix Product Operator constructed from row or column of t tensors in principle is not hermitian – where the (enlarged) edge tensors play the role of the MPS tensors to be truncated, motivating the form of projectors used in (c) and (d). The difference from the MPS procedure is that there the R matrices would correspond to (square roots) of the left and right dominant eigenvectors of MPS transfer matrix which are calculated at every iteration. Here, however, they are found as a result of iterative procedure as CTM is converging. We indeed observe that while CTM procedure is converging, the combined pairs of neighboring corners C are converging to the dominant eigenvectors of the corresponding transfer matrices constructed from opposing edge tensors T .

Finally, we note that in Ref. 8 QR decompositions of the R matrices in (b') are computed and only the upper-triangular parts of those decompositions are retained to calculate the projectors in (c). On paper, this intermediate step does not change the projectors, we see, however, that it indeed increases numerical stability of the CTM algorithm. We perform similar middle step on R^{nw} , R^{ne} obtained in (b), which, for clarity of presentation, is not explicitly shown in Fig. 14.

¹ S. R. White, Phys. Rev. Lett. **69**, 2863 (1992).

² U. Schollwöck, Rev. Mod. Phys. **77**, 259 (2005); Annals of Physics **326**, 96 (2011).

³ F. Verstraete and J. I. Cirac, cond-mat/0407066; V. Murg, F. Verstraete, and J. I. Cirac, Phys. Rev. A **75**, 033605 (2007); G. Sierra and M. A. Martin-Delgado, arXiv:cond-mat/9811170; T. Nishino and K. Okunishi, J. Phys. Soc. Jpn. **67**, 3066 (1998); Y. Nishio, N. Maeshima, A. Gendiar, and T. Nishino, cond-mat/0401115; Z.-C. Gu, M. Levin, and X.-G. Wen, Phys. Rev. B **78**, 205116 (2008); J. Jordan, R. Orús, G. Vidal, F. Verstraete, and J. I. Cirac, Phys. Rev. Lett. **101**, 250602 (2008); H. C. Jiang, Z. Y. Weng, and T. Xiang, *ibid.* **101**, 090603 (2008); Z. Y. Xie, H. C. Jiang, Q. N. Chen, Z. Y. Weng, and T. Xiang, *ibid.* **103**, 160601 (2009); P.-C. Chen, C.-Y. Lai, and M.-F. Yang, J. Stat. Mech.: Theory Exp. (2009) P10001; R. Orús and G. Vidal, Phys. Rev. B **80**, 094403 (2009).

⁴ G. Vidal, Phys. Rev. Lett. **99**, 220405 (2007); **101**, 110501 (2008); L. Cincio, J. Dziarmaga, and M. M. Rams, *ibid.* **100**, 240603 (2008); G. Evenbly and G. Vidal, *ibid.* **102**, 180406 (2009); **112**, 240502 (2014); Phys. Rev. B **79**, 144108 (2009); **89**, 235113 (2014).

⁵ T. Barthel, C. Pineda, and J. Eisert, Phys. Rev. A **80**,

042333 (2009); P. Corboz and G. Vidal, Phys. Rev. B **80**, 165129 (2009); P. Corboz, G. Evenbly, F. Verstraete, and G. Vidal, Phys. Rev. A **81**, 010303(R) (2010); C. V. Kraus, N. Schuch, F. Verstraete, and J. I. Cirac, *ibid.* **81**, 052338 (2010); C. Pineda, T. Barthel, and J. Eisert, *ibid.* **81**, 050303(R) (2010). Z.-C. Gu, F. Verstraete, and X.-G. Wen, arXiv:1004.2563 (2010).

⁶ P. Corboz, R. Orús, B. Bauer, and G. Vidal, Phys. Rev. B **81**, 165104 (2010).

⁷ P. Corboz, S. R. White, G. Vidal, and M. Troyer, *ibid.* **84**, 041108 (2011).

⁸ P. Corboz, T. M. Rice, and M. Troyer, Phys. Rev. Lett. **113**, 046402 (2014).

⁹ P. Corboz, arXiv:1605.03006.

¹⁰ P. Corboz, Phys. Rev. B **93**, 045116 (2016).

¹¹ S. Yan, D. A. Huse, and S. R. White, Science **332**, 1173 (2011).

¹² L. Cincio and G. Vidal, Phys. Rev. Lett. **110**, 067208 (2013).

¹³ S.-J. Ran, W. Li, S.-S. Gong, A. Weichselbaum, J. von Delft, and Gang Su, arXiv:1508.03451.

¹⁴ D. Poilblanc, N. Schuch, D. Pérez-García, and J. I. Cirac, Phys. Rev. B **86**, 014404 (2012).

- ¹⁵ D. Poilblanc and N. Schuch, Phys. Rev. B **87**, 140407(R) (2013).
- ¹⁶ L. Wang, D. Poilblanc, Z.-C. Gu, X.-G. Wen, and F. Verstraete, Phys. Rev. Lett. **111**, 037202 (2013).
- ¹⁷ F. Verstraete, J. J. Garcia-Ripoll, and J. I. Cirac, Phys. Rev. Lett. **93**, 207204 (2004); M. Zwolak and G. Vidal, *ibid.* **93**, 207205 (2004); A. E. Feiguin and S. R. White, Phys. Rev. B **72**, 220401 (2005).
- ¹⁸ S. R. White, arXiv:0902.4475; E. M. Stoudenmire and S. R. White, New J. Phys. **12**, 055026 (2010); I. Pizorn, V. Eisler, S. Andergassen, and M. Troyer, *ibid.* **16**, 073007 (2014).
- ¹⁹ P. Czarnik, L. Cincio, and J. Dziarmaga, Phys. Rev. B **86**, 245101 (2012); P. Czarnik and J. Dziarmaga, *ibid.* **90**, 035144 (2014).
- ²⁰ P. Czarnik and J. Dziarmaga, Phys. Rev. B **92**, 035120 (2015).
- ²¹ A. Molnár, N. Schuch, F. Verstraete, and J. I. Cirac, Phys. Rev. B **91**, 045138 (2015).
- ²² Z. Y. Xie, H. C. Jiang, Q. N. Chen, Z. Y. Weng, and T. Xiang, Phys. Rev. Lett. **103**, 160601 (2009); H. H. Zhao, Z. Y. Xie, Q. N. Chen, Z. C. Wei, J. W. Cai, and T. Xiang, Phys. Rev. B **81**, 174411 (2010); W. Li, S.-J. Ran, S.-S. Gong, Y. Zhao, B. Xi, F. Ye, and G. Su, Phys. Rev. Lett. **106**, 127202 (2011); Shi-Ju Ran, Wei Li, Bin Xi, Zhe Zhang, and Gang Su, *ibid.* **86**, 134429 (2012); S.-J. Ran, B. Xi, T. Liu, and G. Su, *ibid.* **88**, 064407 (2013); A. Denblyker, Y. Liu, Y. Meurice, M. P. Qin, T. Xiang, Z. Y. Xie, J. F. Yu, and H. Zou, Phys. Rev. D **89**, 016008 (2014); H. H. Zhao, Z. Y. Xie, T. Xiang, and M. Imada, arXiv:1510.03333 (2015).
- ²³ Z. Y. Xie, J. Chen, M. P. Qin, J. W. Zhu, L. P. Yang, and T. Xiang, Phys. Rev. B **86**, 045139 (2012).
- ²⁴ K. Takai, K. Ido, T. Misawa, Y. Yamaji, and M. Imada, J. Phys. Soc. Jpn. **85**, 034601 (2016);
- ²⁵ P. Czarnik and J. Dziarmaga, Phys. Rev. B **92**, 035152 (2015).
- ²⁶ P. Czarnik, J. Dziarmaga, and A. M. Oleś, Phys. Rev. B **93**, 184410 (2016).
- ²⁷ Z. Nussinov and J. van den Brink, Rev. Mod. Phys. **87**, 1 (2015).
- ²⁸ S. Wenzel, W. Janke, A. M. Läuchli, Phys. Rev. E **81**, 066702 (2010).
- ²⁹ J. P. F. LeBlanc *et al.*, Phys. Rev. X **5**, 041041 (2015) .
- ³⁰ L. Tagliacozzo, G. Evenbly, and G. Vidal, Phys. Rev. B **80**, 235127 (2009).
- ³¹ R. J. Baxter, J. Math. Phys. **9**, 650 (1968); J. Stat. Phys. **19**, 461 (1978); T. Nishino and K. Okunishi, J. Phys. Soc. Jpn. **65**, 891 (1996); R. Orús and G. Vidal, Phys. Rev. B **80**, 094403 (2009); R. Orús, *ibid.* **85**, 205117 (2012); Ann. of Phys. **349**, 117 (2014); Ho N. Phien, I. P. McCulloch, and G. Vidal, Phys. Rev. B **91**, 115137 (2015).
- ³² R. N. C. Pfeifer, G. Evenbly, S. Singh, and G. Vidal, arXiv:1402.0939.
- ³³ R. T. Scalettar, G. C. Batrouni, Understanding Quantum Phase Transitions, ed. L. Carr, (CRC Press, Boca Raton, 2010) 265.
- ³⁴ D. J. Scalapino, Handbook of High Temperature Superconductivity, ed. J. R. Schrieffer, (Springer, 2007).
- ³⁵ E. Khatami and M. Rigol, Rhys. Rev. A **84** 053611 (2011).
- ³⁶ J. P. F. LeBlanc and E. Gull, Rhys. Rev. B **88** 155108 (2013).
- ³⁷ R. Orús and G. Vidal, Phys. Rev. B **78**, 155117 (2008).
- ³⁸ Y.-K. Huang, P. Chen, and Y.-J. Kao, Phys. Rev. B **86**, 235102 (2012).